MIT Libraries | DSpace@MIT

MIT Open Access Articles

Lunar impact basins revealed by Gravity Recovery and Interior Laboratory measurements

Massachusetts Institute of Technology

PLANETARY SCIENCE

Lunar impact basins revealed by Gravity Recovery and Interior Laboratory measurements

Gregory A. Neumann,[1]* Maria T. Zuber,[2] Mark A. Wieczorek,[3] James W. Head,[4] David M. H. Baker,[4] Sean C. Solomon,[5,6] David E. Smith,[2] Frank G. Lemoine,[1] Erwan Mazarico,[1] Terence J. Sabaka,[1] Sander J. Goossens,[7] H. Jay Melosh,[8] Roger J. Phillips,[9] Sami W. Asmar,[10] Alexander S. Konopliv,[10] James G. Williams,[10] Michael M. Sori,[2†] Jason M. Soderblom,[2] Katarina Miljković,[2‡] Jeffrey C. Andrews-Hanna,[11] Francis Nimmo,[12] Walter S. Kiefer[13]

Observations from the Gravity Recovery and Interior Laboratory (GRAIL) mission indicate a marked change in the gravitational signature of lunar impact structures at the morphological transition, with increasing diameter, from complex craters to peak-ring basins. At crater diameters larger than ~200 km, a central positive Bouguer anomaly is seen within the innermost peak ring, and an annular negative Bouguer anomaly extends outward from this ring to the outer topographic rim crest. These observations demonstrate that basin-forming impacts remove crustal materials from within the peak ring and thicken the crust between the peak ring and the outer rim crest. A correlation between the diameter of the central Bouguer gravity high and the outer topographic ring diameter for well-preserved basins enables the identification and characterization of basins for which topographic signatures have been obscured by superposed cratering and volcanism. The GRAIL inventory of lunar basins improves upon earlier lists that differed in their totals by more than a factor of 2. The size-frequency distributions of basins on the nearside and farside hemispheres of the Moon differ substantially; the nearside hosts more basins larger than 350 km in diameter, whereas the farside has more smaller basins. Hemispherical differences in target properties, including temperature and porosity, are likely to have contributed to these different distributions. Better understanding of the factors that control basin size will help to constrain models of the original impactor population.

INTRODUCTION

Impact basins (1), large circular structures characterized by two (peak-ring basins) or more (multiring basins) concentric topographic rings (2–4), have long been recognized on the Moon. Imaging and topographic mapping permitted the determination of basin ring dimensions, spacing, and morphology and elucidated how these characteristics change with increasing basin size (1–7). Stratigraphic relationships and the size-frequency distribution of smaller superposed impact craters provided a basis for a relative chronology of basin-forming events (5), but this chronology was inevitably incomplete because of the destructive effects of superposed impacts and volcanic resurfacing. These effects also obscured the evidence for the processes responsible for the formation of multiple rings with increasing impactor size (1, 4–11).

With the origin of basin rings uncertain, relations among the basin diameter, the size of the transient crater that forms in the initial stages of basin formation, and the impact conditions (impactor size, velocity, and impact angle) have remained elusive (12).

The discovery and early documentation of positive free-air gravity anomalies in areas of low elevation within basin interiors (13) (that is, mass concentrations or mascons) provided a connection between crustal structure and the transition with increasing diameter from impact craters to basins. Mascons were attributed to both the upward displacement of the crust-mantle interface and the partial filling of the basin cavity by mare basalts that are denser than the surrounding crustal material (14, 15). Refinements to the lunar gravity field (16–18) led to further studies of the deep structure of the largest (>600-km-diameter) lunar basins (12, 19, 20), but the underlying structure of many smaller peak-ring basins remained unresolved, particularly on the farside hemisphere of the Moon where such structures have not been obscured by mare fill but where the gravity field could not be directly derived from line-of-sight tracking from Earth.

NASA's Gravity Recovery and Interior Laboratory (GRAIL) mission has obtained a globally accurate lunar gravity field (21) that resolves the major structural elements of both fresh and degraded impact basins. We subtract the predominantly short-wavelength gravity signal attributable to surface topography (22) from the observed lunar gravity field to obtain the Bouguer anomaly (Fig. 1), which reveals the subsurface variations in crustal thickness and/or density arising from basin-forming impacts. Peak-ring and multiring basins, as well as many proposed basins, may be recognized by their distinctive circular outlines in this map view, refined from earlier mission results (21). For example, Fig. 2 shows the two topographic rings and prominent axisymmetric regions of positive and negative Bouguer gravity anomalies for a typical farside impact structure, the 582-km-diameter Freundlich-Sharonov basin. The interior peak ring encloses a region of positive Bouguer anomaly,

[1]Solar System Exploration Division, NASA Goddard Space Flight Center, Greenbelt, MD 20771, USA. [2]Department of Earth, Atmospheric and Planetary Sciences, Massachusetts Institute of Technology, Cambridge, MA 02139, USA. [3]Institut de Physique du Globe de Paris, Sorbonne Paris Cité, Université Paris Diderot, CNRS, Paris 75013, France. [4]Department of Earth, Environmental and Planetary Sciences, Brown University, Providence, RI 02912, USA. [5]Lamont-Doherty Earth Observatory, Columbia University, Palisades, NY 10964, USA. [6]Department of Terrestrial Magnetism, Carnegie Institution of Washington, Washington, DC 20015, USA. [7]Center for Research and Exploration in Space Science and Technology, University of Maryland, Baltimore County, Baltimore, MD 21250, USA. [8]Department of Earth, Atmospheric, and Planetary Sciences, Purdue University, West Lafayette, IN 47907, USA. [9]Planetary Science Directorate, Southwest Research Institute, Boulder, CO 80302, USA. [10]Jet Propulsion Laboratory, California Institute of Technology, Pasadena, CA 91109–8099, USA. [11]Department of Geophysics and Center for Space Resources, Colorado School of Mines, Golden, CO 80401, USA. [12]Department of Earth and Planetary Sciences, University of California, Santa Cruz, Santa Cruz, CA 95064, USA. [13]Lunar and Planetary Institute, Houston, TX 77058, USA.
*Corresponding author. E-mail: Gregory.A.Neumann@nasa.gov
†Present address: Lunar and Planetary Laboratory, University of Arizona, Tucson, AZ 85271, USA.
‡Present address: Department of Applied Geology, Curtin University, GPO Box U1987, Perth, WA 6845, Australia.
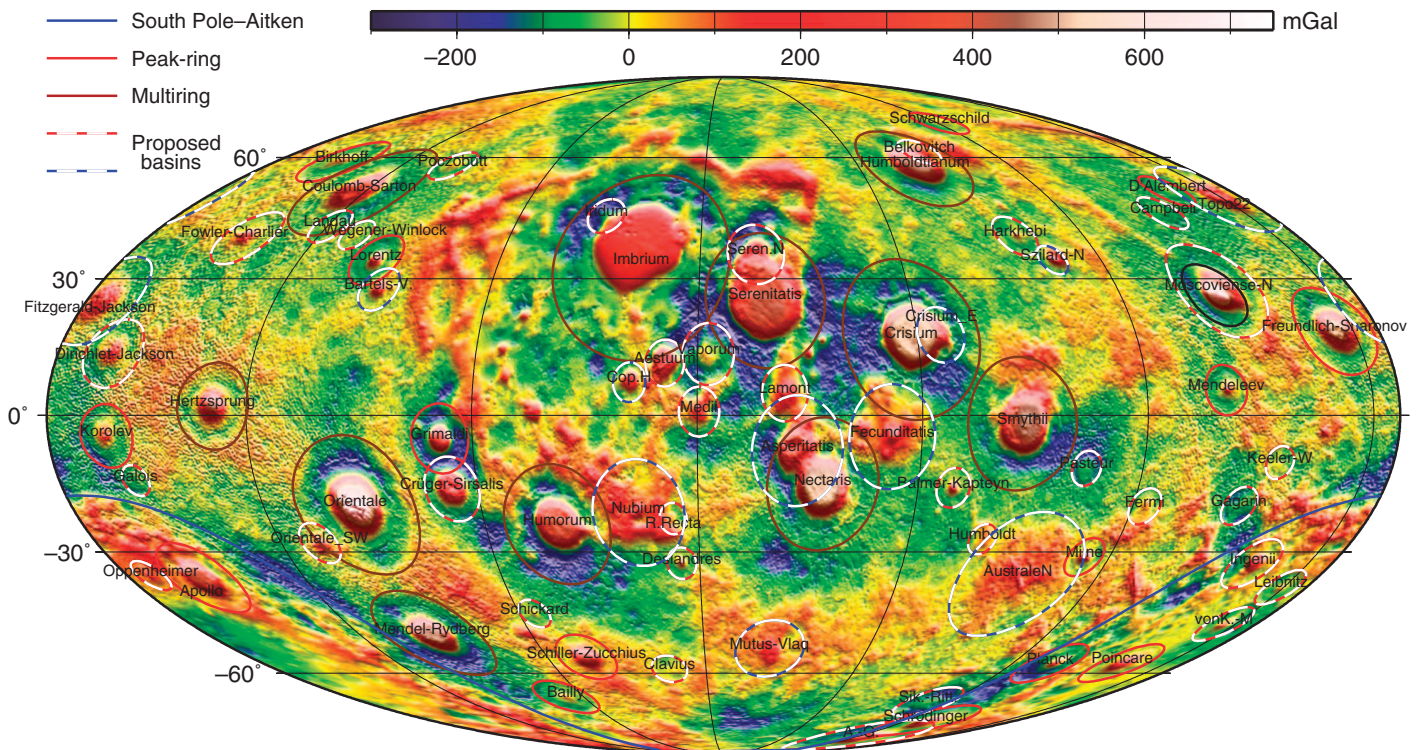
Fig. 1. Bouguer anomaly map for the Moon. A color-contoured map of the Bouguer-corrected GRAIL gravity anomaly, in Mollweide equal-area projection centered on the nearside at 7°E longitude, band-passed between ~10- and 900-km block size and hill-shaded from above. The Bouguer anomaly scale is in mGal (milliGalileo; 10^{-5} m s^{-2}). Over spherical harmonic degrees 6 to 540, the band-pass window predominantly removes the effect of the hemispheric asymmetry and the South Pole–Aitken impact and allows identification of impact basins up to the size of Imbrium. Red/white circles show proposed basins having only one topographic ring and no interior peak ring or central peak but a gravity signature similar to those of peak-ring basins. Blue-white circles outline basins that lack a clearly defined topographic rim crest but that are suggested by gravity anomaly patterns to be basins (see the Supplementary Materials for details).

whereas the topographic rim crest encloses an annulus of negative Bouguer anomaly. Outside the basin rim, the Bouguer anomaly approaches zero. The positive and negative anomalies are interpreted in cross section (Fig. 2C) as regions of thinned and thickened crust, respectively (23), that are bounded by the inner and outer rings. The central thinned crust and surrounding annulus of thickened crust are a result of crater excavation and collapse predicted by numerical simulations of the cratering process (24). Hydrocode simulations of the basin-forming process show that peak rings form after the rebound and collapse of the basin interior (10, 25), but, as of yet, no hydrocode model has directly reproduced the outer rings. The GRAIL gravity data now link the subsurface structure of a basin to its observed surface expression, allowing for more complete characterization of the size, number, and distribution of lunar impact basins.

RESULTS

Gravity and basin morphology

With topography from the Lunar Orbiter Laser Altimeter (LOLA) (22), we compared lunar gravity and basin morphology for 16 well-preserved peak-ring basins (7) and all similar-sized craters with rim-crest diameters larger than 160 km, with or without additional rings. A distinct transition in morphology with increasing diameter is seen at a diameter

of about 200 km, from that of smaller complex craters—with relatively deep floors, terraced walls, and often a prominent central peak—to that of larger but shallower (relative to their size) basins with or without a peak ring and no central peak (7). A corresponding transition in the gravitational signature is also found. We examined the amplitude and size of the central positive Bouguer anomaly as seen in Fig. 2B as a measure of the degree of crustal thinning. Our survey shows that in well-preserved basins where a peak ring is present, the central positive Bouguer anomaly is always enclosed by the innermost ring, and the annulus of negative Bouguer anomaly extends from this ring to the main topographic rim crest. The contrast between the annular negative and central positive anomalies increases with increasing basin diameter, commencing at ~200 km and continuing up to and beyond the transition to multiring basins at about 500 km (Fig. 3) (the diameters of multiring basins are assessed in the Supplementary Materials). Smaller complex craters with diameters from 160 to 200 km but without multiple rings have modest or even slightly negative Bouguer anomaly contrasts, the result of variations in crustal density from that assumed. The increase in the Bouguer anomaly contrast with increasing diameter occurs for nearside and farside impact structures, but other factors such as age, thickness of mare fill, crustal thickness, and background thermal state (19, 26, 27) must also contribute because the correlation with size is only moderate. The highest Bouguer anomaly contrast occurs for Orientale, the youngest major impact basin. The oldest and largest basin,
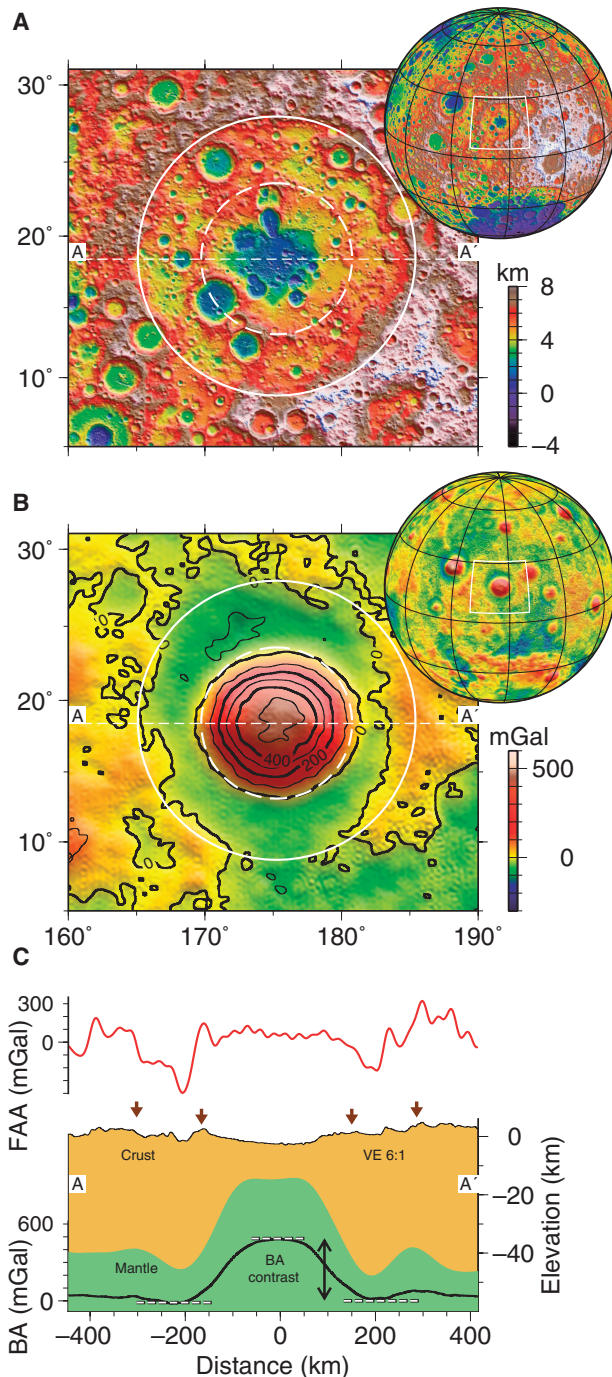
Fig. 2. Freundlich-Sharonov basin. (**A**) Topography of this farside peak-ring basin is shown over shaded relief. Inset: Location of the region. Solid (582-km-diameter) and dashed (318-km-diameter) circles mark the rim crest or main ring and inner peak ring, respectively. (**B**) Bouguer gravity anomaly map band-passed between ~10- and 900-km block size, directionally shaded. The Bouguer gravity anomaly contour interval is 100 mGal. (**C**) Cross-sectional diagram of the topography, free-air anomaly (FAA), Bouguer anomaly (BA), and crustal structure (23) along profile A–A'. Vertical exaggeration (VE) is 6:1. Arrows denote the locations of the outer rim crest and inner peak ring. Dashed lines illustrate Bouguer contrast between spatial averages over the central (from 0 to 20% of the rim radius) and annular (50 to 100%) regions.
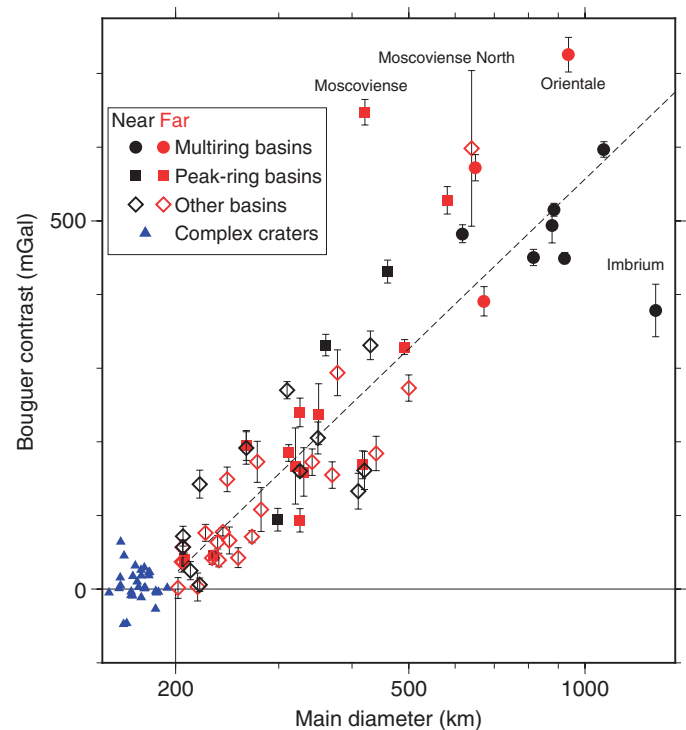

Fig. 3. Bouguer anomaly contrast versus main ring diameter (log scale). Symbols show complex craters >160 km in diameter (blue triangles), nearside basins (black symbols), and farside basins (red symbols). Open symbols represent possible basins in which multiple rings are not preserved. The rate of increase in Bouguer anomaly contrast given by a log-linear least-squares fit to diameter (dashed line) is about 240 mGal per factor of 2 increase in diameter. Moscoviense is believed to be a double impact (41) and is plotted as two separate points, Moscoviense and Moscoviense North.

the South Pole–Aitken basin, is not shown here, because its size is comparable to the band-pass filter we applied to the gravity data (see Materials and Methods).

The diameter of the central Bouguer anomaly is plotted versus the diameter of the innermost basin ring in Fig. 4. For peak-ring basins, the former diameter is about equal to that of the peak ring for all but the two smallest basins shown. The size of the central Bouguer anomaly is also comparable to the diameters of the innermost topographic rings of multiring basins (excluding the "inner depression" ring; see the Supplementary Materials). The trends of Bouguer anomaly contrast and size are similar for both peak-ring and multiring basins, suggesting that the innermost ring of a multiring basin is equivalent to the peak ring of smaller basins.

One basin for which the innermost ring diameter is difficult to assess is Serenitatis. The innermost 420-km-diameter Linné ring defined by concentric wrinkle ridges in the mare does not entirely enclose the central positive Bouguer anomaly, of which the well-preserved southern portion instead lies within a larger 660-km-diameter Haemus ring (fig. S1), which we interpret to represent the Serenitatis peak-ring equivalent.

The diameter of the peak ring or its closely corresponding diameter of mantle uplift guides the selection of the rim crest of multiring basins, for which many topographic rings have been proposed. A long-known relation for peak-ring basins such as Schrödinger is that the diameter of
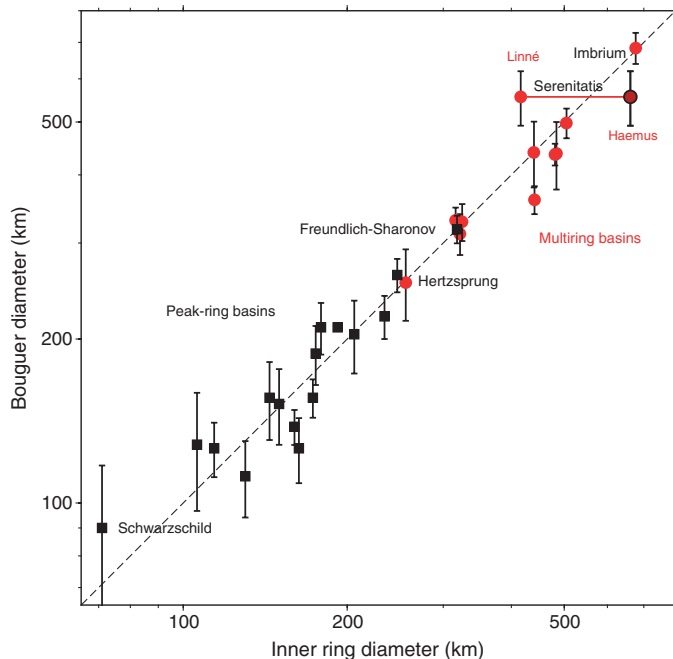
Fig. 4. Diameter of the central positive Bouguer anomaly versus diameter of the peak ring or inner topographic ring. The 16 peak-ring (black) and 11 multiring (red) basins identified in this and previous studies (*7*) are shown. Identification of the inner ring of the Serenitatis basin (fig. S1) is uncertain owing to later modification. Both a 660-km-diameter Haemus ring and a 420-km-diameter Linné ring (both named for topographic features along the rings) are shown connected by a red line. The dashed line indicates a 1:1 ratio.

the main topographic rim is about twice the peak-ring diameter [this relation also holds for peak-ring basins on Mars, Mercury, and Venus (*7–10*)]. Where multiple rings are present, we chose the ring that is nearly concentric with and closest to twice the Bouguer anomaly diameter to represent the basin diameter (see the Supplementary Materials). The annulus of negative Bouguer anomaly is always found to be confined within the main basin ring, just as it is for smaller peak-ring basins. For the most probable multiring basins, the negative Bouguer anomaly is centered on the intermediate topographic ring that lies between the peak ring and main rim crest. For depressions that lack confidently measureable rings but are suggested by GRAIL to be degraded basins, we estimate a main ring diameter from the circular portions of the Bouguer anomaly for analysis of the population statistics and inferred impact energy of craters.

Assessment of newly identified and previously proposed basins

The correspondence between gravitational signature and basin morphology provides a basis for the identification and characterization of basins for which the topographic signature has been obscured by subsequent crater formation and allows us to determine the extent to which the population of basins defined by morphological characteristics is accurate and complete. Given the relations between the diameters of the peak ring and the main basin rim (*7, 9*) and between the diameters of the central Bouguer anomaly and the peak ring (Fig. 4), we searched for missing basins, assessed the characteristics of proposed basins,

and determined the main ring diameters of previously known but degraded basins, as summarized in Table 1 with additional details in tables S1 to S7.

Among all craters and degraded circular impact structures, including some recently proposed (*28, 29*), there are 3 certain, 4 probable, and 4 possible multiring basins, described in detail in tables S2 and S3, along with the 16 previously identified peak-ring basins (table S4) (*7*). We confirm 30 other previously known impact structures with only one topographic ring, 28 of which are comparable in size, morphology, and gravity signature (table S5) to known peak-ring basins. All but four have positive Bouguer contrasts exceeding 35 mGal, a result suggesting that 24 of this last group of structures may originally have formed with an interior peak ring that was later rendered unrecognizable by ejecta from younger basins, superposed craters, and/or mare infill. Therefore, the global population of peak-ring basins is substantially greater than that of the well-preserved examples. Less well-preserved basins include both older and highly degraded peak-ring basins such as Fitzgerald-Jackson (*29*) shown in fig. S2 and relatively younger candidates obscured by ejecta from large nearby impacts (for example, Amundsen-Ganswindt, a heavily altered basin just southwest of the 326-km-diameter Schrödinger basin, fig. S3).

GRAIL gravity data confirm the existence of 16 additional basins that lack confidently measurable topographic rings but that have Bouguer anomaly signatures that are typical of peak-ring basins (table S6). Thirteen of these features have previously been proposed to be basins on the basis of broad topographic and crustal thickness anomalies, whereas three (Asperitatis, Bartels-Voskresenskiy, and Copernicus-H) (figs. S4 to S6) are newly identified in this work. The known relations among the diameters of a peak ring, the central Bouguer anomaly, and the main basin rim allow us to estimate the approximate size of these basins. We also assessed the topography and gravity anomalies in the vicinity of 71 basins that have previously been proposed in the literature (table S7), but on the basis of their unconvincing topographic expressions and their lack of a distinctive peak-ring Bouguer anomaly signature, we cannot confirm those identifications.

The cumulative size-frequency distribution $N(D)$ of the lunar craters and basins confirmed in this study, where D is the estimated diameter in kilometers of the main topographic rim crest or the main ring of multiring basins and N is the number of craters with diameter larger than D per unit area, is shown in Fig. 5. The size-frequency distribution of craters and basins smaller than 200 km is virtually the same as the earlier Hartmann power-law production function (*30*), but we obtain $N(300) = (1.1 \pm 0.15) \times 10^{-6} \, \text{km}^{-2}$, a value slightly larger than a commonly used Apollo-era estimate of $0.92 \times 10^{-6} \, \text{km}^{-2}$ (*5*). For diameters larger than 300 km, this study yields substantially more basins than the LOLA-derived population (*6*), as shown in a normalized plot (Fig. 6). However, our value of $N(300)$ is a factor of 2.3 smaller than a recent estimate (*28*) derived from Clementine topography and Lunar Prospector gravity.

Important hemispherical-scale differences in the size-frequency distribution of basins are observed. Relatively more basins with diameters larger than 350 km are found on the nearside hemisphere than on the farside. This observation has been suggested to be a consequence of elevated nearside temperatures in the Procellarum KREEP Terrane that causes impact craters to form larger diameters, for a given impact energy, than those on the colder farside crust (*27, 31*). In contrast, the farside has a relative surplus of basins with $D < 300$ km. The farside hosts 13 of the 16 peak-ring basins, and even when the number of

Table 1. Lunar basins ≥200 km in diameter recognized from GRAIL and LOLA data. Names are approved by the International Astronomical Union, except where denoted by ([a]), indicating a name assigned here on the basis of a nearby feature, or ([b]), a proposed name (5, 29). TOPO and CTA (circular thin area) names are from Frey (28). The diameter of the main or outer ring is from Head *et al.* (6) and Baker *et al.* (7) except where a mappable rim is absent, for example, Crüger-Sirsalis; otherwise, coordinates and inner diameter are estimated from Bouguer anomaly contours, whereas the main rim crest diameter is estimated from azimuthally averaged topographic relief or ([c]) inferred from the diameter of the central Bouguer anomaly by 2:1 scaling. Multiring basin confidence and ring diameter criteria are described in the Supplementary Text. Ring confidence is denoted by the following: { }, suggested by scaling; [ ], possible; ( ), probable; all others, certain. MR, multiring basin; PC, ringed peak-cluster basin (7); PR, peak-ring basin; ghost ring is a wrinkle-ridge arc indicating a possible buried ring.

Name	Center		Ring diameters (km)			Bouguer anomaly	
	Latitude (°N)	Longitude (°E)	Main	Inner	Notes and additional ring diameters (km)	Diameter (km)	Contrast (mGal)
Szilard North[a]	34.3	105.6	(200)			146	182 ± 20
Bel'kovich	61.5	90.2	205			104	37 ± 14
Wegener-Winlock[b]	40.2	251.6	(205)		PR*	132	37 ± 6
Humboldt	−27.15	81	206		PC	156	52 ± 14
Oppenheimer	−35.4	194.0	206		PR*	122	57 ± 8
Schickard	−44.5	305.0	206		PR*	92	57 ± 9
Schwarzschild	70.3	121	207	71	PR	90	40 ± 9
Galois	−14	207.7	210		Minimal contrast		2 ± 14
Rupes Recta[a]	−22.5	353.0	(212)		Partially flooded		25 ± 12[†]
Keeler West	−10.1	156.8	(218)		Minimal contrast		5 ± 20[†]
Clavius	−58.8	345.3	220		Minimal contrast		6 ± 9
Deslandres	−32.6	354.7	220		PR*	112	142 ± 19
TOPO-13[b]	−37.25	147.4	[220]			90	103 ± 12
Poczobutt	57.7	260.4	225		PR*	128	76 ± 12
Pasteur	−11.5	104.8	231		PR*	130	42 ± 9
d'Alembert	51.05	164.8	232	106	PR	126	46 ± 6
Landau	42.2	240.8	236		PR*	112	64 ± 9
Campbell	45.5	153.0	237		PR*	98	39 ± 9
Fermi	−19.8	123.4	241		PR*	104	78 ± 5
Leibnitz	−38.2	179.2	247		PR*	84	66 ± 18
Iridum[a]	44.8	328.4	252		Sinus Iridum, PR*		38 ± 10[†]
von Kármán M	−47.1	176.2	255	[114]	PR*	128	149 ± 18
Gagarin	−19.7	149.4	256		PR*	106	43 ± 13
Copernicus-H[a]	7.2	341.8	{260}[c]	[130][c]		152	162 ± 5
Milne	−31.25	112.8	264	114	PR	126	195 ± 22
Balmer-Kapteyn[b]	−15.8	69.6	265	[130]	PR*	138	192 ± 22
Sikorsky-Rittenhaus[b]	−68.4	109.5	270	[110]	PR*	106	66 ± 8
Orientale Southwest[a]	−28.0	251.0	276		PR*	162	173 ± 28
Harkhebi	40.0	98.6	280		PR*	136	108 ± 30
Bartels-Voskresenskiy[a]	27.7	268.2	[290]	[160]	PR*	152	197 ± 22
continued on next page							

Name	Center		Ring diameters (km)			Bouguer anomaly	
	Latitude (°N)	Longitude (°E)	Main	Inner	Notes and additional ring diameters (km)	Diameter (km)	Contrast (mGal)
Bailly	−67.1	291.1	299	130	PR	112	94 ± 16
Poincare	−57.3	163.1	312	175	PR	188	185 ± 11
Planck	−57.4	135.1	321	160	PR	128	167 ± 52
Medii[a]	0.8	0.5	[326]		Sinus Medii; CTA-01	174	160 ± 8
Schrödinger	−74.9	133.5	326	150	PR	154	240 ± 19
Aestuum[a]	11.3	351.1	[330]	[165]	Sinus Aestuum; CTA-25; PR*	196	268 ± 10
Mendeleev	5.5	141.1	331	144	PR	156	159 ± 33
Birkhoff	58.9	213.4	334	163	PR	130	90 ± 16
Ingenii	−32.8	163.8	342		PR*	154	181 ± 22
Lorentz	34.2	263.0	351	173	PR	156	240 ± 38
Schiller-Zucchius	−55.7	314.8	361	179	PR	210	331 ± 15
Lamont	4.8	23.4	[370][c]	[120]	Ghost ring	206	213 ± 23
Crisium East[a]	16.5	66	[372]	[186]	Possible oblique impact; TOPO-05	206	339 ± 45[†]
Fowler-Charlier[b]	39.5	218.0	[374]		PR*	210	156 ± 18
Amundsen-Ganswindt[b]	−81.0	123.0	378		PR*	170	272 ± 46
Vaporum[b]	14.2	3.1	[410]	220	Mare; CTA-02	222	120 ± 24
Korolev	−4.4	202.2	417	206	PR	202	173 ± 15
Serenitatis North[a]	35.7	16.8	[420][c]	[210]		230	161 ± 26
Moscoviense	26.1	147	421[‡]	192	PR		632 ± 27[†]
Crüger-Sirsalis[b]	−16.0	293.0	[430][c]	212	PR*	268	331 ± 19
Mutus-Vlacq	−53.5	24.0	[450][c]	{225}		224	107 ± 13
Dirichlet-Jackson[b]	13.4	201.8	(452)	[228]	PR*; TOPO-24	220	182 ± 22
Grimaldi	−5.0	291.3	460	234	PR	220	431 ± 15
Apollo	−36.1	208.3	492	247	PR	264	329 ± 10
TOPO-22[a]	49.4	179	{500}	[250][c]	Depression near Debye	272	274 ± 21
Hertzsprung	2.0	231	571	256	MR intermediate (408), inner depression (108)	254 ± 38	404 ± 37
Freundlich-Sharonov[b]	18.35	175.2	582	318	PR	318	528 ± 18
Fitzgerald-Jackson[b]	25.1	190.6	{600}	(346)		334	224 ± 48
Humboldtianum	57.26	82	618	322	Possible MR intermediate [463], [197]	312 ± 27	482 ± 12
Moscoviense North[a]	27.3	148.8	640[‡]	[340]	PR*; double impact (65)		
Mendel-Rydberg[b]	−49.8	265.4	650	(325)	MR 485, 203	328 ± 26	572 ± 18
Coulomb-Sarton[b]	51.2	237.5	[672]	315	Possible MR (401), 158	330 ± 18	391 ± 20
Fecunditatis	−4.6	52.0	[690]	{345}	Mare basin	358	205 ± 46
Nubium	−21.3	343.4	[690]		Mare basin, estimates vary	416	81 ± 41
Asperitatis[a]	−7.7	26.8	{730}[c]	(345)[c]	Sinus name	342	260 ± 26
Humorum	−23.8	320.8	816	441	Probable MR (569), (322)	360 ± 21	450 ± 11
continued on next page							

Name	Center		Ring diameters (km)			Bouguer anomaly	
	Latitude (°N)	Longitude (°E)	Main	Inner	Notes and additional ring diameters (km)	Diameter (km)	Contrast (mGal)
Smythii	−2.5	86.9	878	484	Probable MR (375)	438 ± 62	494 ± 24
Australe North[a]	−35.5	96	{880}		Mare basin	538	101 ± 22
Nectaris	−15.6	35.1	885	440	Certain MR 623, (270)	440 ± 61	514 ± 12
Serenitatis	25.4	18.8	[923]	[416]	Possible MR 660	556 ± 64	450 ± 8
Orientale	−20.1	265.2	937	481	Certain MR 639, 341	436 ± 20	720 ± 28
Crisium	16.8	58.4	1076	505	Probable MR 809, (364)	498 ± 31	598 ± 10
Imbrium	37	341.5	1321	676	Probable MR (1012)	684 ± 45	375 ± 37
South Pole–Aitken[b]	−53.0	191.0	2400	2028	Elliptical shape, 19°W long axis		395

*The topographic rim is in the diameter range of peak-ring basins but no inner ring has been preserved. †Contrast estimate from nonoverlapped portion. The estimated Bouguer anomaly contrast for South Pole–Aitken is taken from a gravity field band-passed from spherical harmonic degrees 1 to 540. ‡The characteristics of a pre-Moscoviense impact, designated Moscoviense North, are further described in the Supplementary Materials.
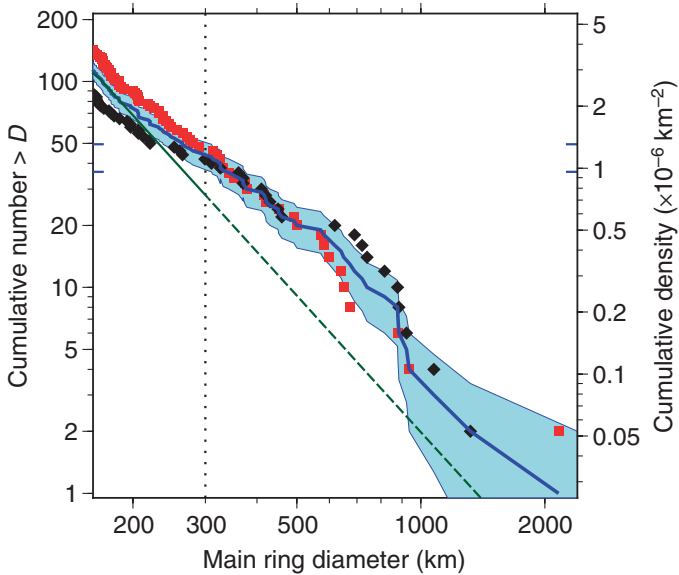
Fig. 5. Cumulative size-frequency distribution for complex craters and basins. The blue line shows data for all the craters and basins in Table 1. The shaded region spans the 1-SD error estimates. Black diamonds and red squares show the cumulative size-frequency distributions for near-side and farside craters, respectively, normalized by area; for these symbols, the cumulative number scale on the left reads two times the value. Short horizontal blue lines show confidence limits of N(300) for the overall population. The cumulative Hartmann production function (30) for craters larger than 64 km is shown by the green line with a slope of −2.2, extrapolated for diameters larger than 300 km (vertical dotted line). The main ring diameter was inferred from the diameter of the central Bouguer anomaly high for basins observed in GRAIL data that lack an outer topographic rim.

Fig. 6. Relative size-frequency distribution of lunar craters and basins. Logarithmic plot of relative frequency R of craters in this study (blue circles) versus the geometric mean d of diameters in each size bin. Bin boundaries from b_1 to b_2 containing N craters range from $2^{4.5}$ to $2^{11.5}$ km by multiples of $\sqrt{2}$. The frequencies are normalized to $R = d^3N/[A(b_2 - b_1)]$, where A is the surface area of the Moon. The data set in this study contains substantially more features of a given size than the database of Head et al. (6) (brown diamonds, 1-SD confidence shaded in pink), except in the interval centered on 214 km where the "Keeler-Heaviside" and "TOPO-19" features did not meet our criteria for inclusion. Green squares illustrate the size distribution of main-belt asteroids from the Sloan Digital Sky Survey [after Strom et al. (38), Fig. 4], normalized in scale to match the relative values of the lunar crater population at a diameter of 100 km.

nearside peak-ring basins is corrected for the area resurfaced by mare basalt deposits, there are still more than twice as many peak-ring basins on the farside hemisphere than on the nearside. Furthermore, 16 of 24 basins that have only one topographic ring and no interior peak ring or central peak structure but a distinct peak-ring-like gravity anomaly pat-
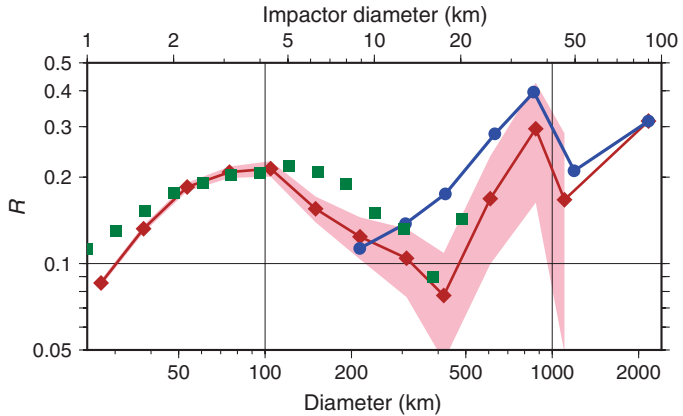
tern (table S5) are found on the farside. Combining both groups, 29 of 40 such basins are found on the farside. The probability that 29 or more basins of the total population are concentrated in either hemisphere by random chance is <1%. The difference in the distribution of the peak-ring basins between the nearside and farside is robust; even if four additional peak-ring basins were hidden beneath nearside maria, or if four farside identifications were false, the probability of chance occurrence would be <5%; moreover, we did not include several other poorly pre-served farside basins, such as Fitzgerald-Jackson, that resemble peak-ring basins.

DISCUSSION

GRAIL gravity data in combination with high-resolution topography have revealed in great detail the population and three-dimensional structure of lunar impact basins. For the diameter range from 200 to 1000 km, the regions of crustal thinning and thickening revealed by Bouguer gravity anomalies are closely coupled to basin ring structures, providing a new constraint on simulations of the impact process and the formation of multiring basins. Such simulations must eventually reproduce the observed scaling relationships (Figs. 2 and 3).

Hemispherical differences in the distribution of the largest basins may be the result of lateral variations in crustal temperature (27), but hemispherical differences in smaller peak-ring basins are not explained by this mechanism. The transition diameter from craters to basins and the Bouguer anomaly contrast with increasing basin diameter (Fig. 3) do not substantially differ between the nearside and farside hemispheres, between thicker and thinner crust, or among the major crustal provinces (32), nor does the hemispherical difference in the number of peak-ring basins result from spatial variations in the impact flux (33). Wilhelms (5) argued that most basins are pre-Nectarian in stratigraphic age. Given that the farside has the greatest pre-Nectarian surface area, one could argue that the hemispheric difference is the result of age, but GRAIL data are less affected by subsequent impacts and obscuration by lava flooding and should reveal a more balanced population. One could also argue that viscous relaxation is important to the loss of discernible basins in the Procellarum KREEP Terrane, but its area is too small to account for the entire difference. Thermal effects are important for larger basins, but not important for smaller peak-ring-like basins (27).

One contributing factor for the observed hemispheric asymmetry in the number of peak-ring basins could be the presence of a highly fractured thick ejecta blanket on the farside crust that was emplaced during the formation of the South Pole–Aitken basin (15). The relationship between impact conditions (that is, bolide size and velocity) and final crater diameter is known to depend on porosity, with porous sand-like targets yielding smaller craters than nonporous targets (34). Extrapolation of these relations to peak-ring basin sizes predicts a difference in diameter that could be as large as 40%. Although a sand-like target for the entire lunar crust is not realistic, the experimental data for intermediate porosities are limited.

Previous investigations of the early impact bombardment of the Moon suffered from an incomplete catalog of impact basins and uncertainty regarding their size and subsurface structure (5). These deficiencies have affected estimates of the cratering flux and crater retention ages for the other terrestrial planets, because it is the lunar cratering rate that anchors the impact chronology for the entire inner solar system (34). The size-frequency distribution of large lunar impact basins is now better constrained, particularly for the oldest and most degraded structures. Six basins are estimated to be at least 200 km larger in diameter than in a previous database (6), a result of differences in the interpretations of the various basin rings. The distinctive Bouguer gravity signature of peak-ring basins and their more degraded analogs permits the construction of a cumulative size-frequency distribution with greater confidence.

Several models for the late heavy bombardment of the inner solar system during which many lunar basins formed have invoked processes that disrupted objects in the main asteroid belt (35, 36). However, attempts to reproduce the observed distribution of basins from the size distributions of objects in the main asteroid belt with Monte Carlo experiments (37) have encountered difficulties. Calibrating the population of impactors to the observed population of ~100-km-diameter craters leads to an underestimate of the population of basins ~300 to 1200 km in diameter but predicts an excess population of basins larger than Imbrium, of which only one (South Pole–Aitken) is known. Because of an increase in the number of large (>300 km in diameter) basins recognized in this work (Fig. 5), the GRAIL measurements worsen the fit of basin size distributions to the size distribution of main-belt asteroids (38). Moreover, GRAIL data do not reveal such a family of impacts larger than Imbrium, other than the South Pole–Aitken basin. The gravitational signature of such large impacts is not apparent even in maps of Bouguer anomalies that have not been band-passed. Thus, this study supports the inference (37) that most lunar basins did not form from objects having a size distribution matching that of modern main-belt asteroids.

MATERIALS AND METHODS

In a principal axis coordinate system identical to that in which the gravity data are presented, the LOLA topography (22) was used in combination with the GRGM900C gravity model (39) to compute the spherical harmonic coefficients of the Bouguer potential with a reference radius of 1738 km via a finite-amplitude expansion (40). To exclude hemispheric-scale, long-wavelength effects and short-wavelength noise, we obtained a map by filtering from degrees 6 to 540. The gravitational attraction of the surface relief was calculated for a crustal density of 2500 kg m^{-3}, and the possible contribution of denser mare basalts was neglected. The diameter of the central Bouguer anomaly is that for which the azimuthally averaged Bouguer anomaly exceeds its baseline value, taken as the 60% quantile of the Bouguer anomaly distribution within the basin diameter. The uncertainty is derived from the dependence on the baseline value from the 50% to the 70% quantile. The Bouguer anomaly contrast is the difference between the innermost average and the average within the outer annulus, from 0 to 20% and from 50 to 100% of the rim radius, respectively, as illustrated in Fig. 2C. Error bars are 1 SD of the variations within the central region. Latitudes and longitudes are given in planetocentric (east positive) coordinates, and gravity anomalies are positive downward, completing a right-hand coordinate system.

SUPPLEMENTARY MATERIALS

Supplementary material for this article is available at http://advances.sciencemag.org/cgi/content/full/1/9/e1500852/DC1

Supplementary Text
Morphology and morphometry of impact basins
Maps of impact basins
Multiring basins
Peak-ring basins and other sizeable lunar impacts
Basins without measurable rings that are identifed by GRAIL Bouguer gravity anomaly
Fig. S1. Serenitatis, Serenitatis North, and Lamont.
Fig. S2. Fitzgerald-Jackson.
Fig. S3. Amundsen-Ganswindt and Schrödinger.
Fig. S4. Nectaris and Asperitatis.
Fig. S5. Lorentz and Bartels-Voskresenskiy.
Fig. S6. Copernicus-H and Aestuum.
Fig. S7. Orientale and Orientale Southwest.
Fig. S8. Mendel-Rydberg.
Fig. S9. Imbrium and Iridum.
Fig. S10. Crisium and Crisium East.
Fig. S11. Humorum.

REFERENCES AND NOTES

1. W. K. Hartmann, G. P. Kuiper, Concentric structures surrounding lunar basins. *Commun. Lunar Planet. Lab.* **1**, 51–66 (1962).
2. W. K. Hartmann, C. W. Wood, Moon: Origin and evolution of multi-ring basins. *Moon* **3**, 3–78 (1971).
3. R. J. Pike, Depth/diameter relations of fresh lunar craters: Revision from spacecraft data. *Geophys. Res. Lett.* **1**, 291–294 (1974).
4. P. D. Spudis, *The Geology of Multi-ring Basins* (Cambridge Univ. Press, Cambridge, 1993).
5. D. E. Wilhelms, *The Geologic History of the Moon* (U.S. Geological Survey Professional Paper 1348, Government Printing Office, Washington, DC, 1987).
6. J. W. Head III, C. I. Fassett, S. J. Kadish, D. E. Smith, M. T. Zuber, G. A. Neumann, E. Mazarico, Global distribution of large lunar craters: Implications for resurfacing and impactor populations. *Science* **329**, 1504–1507 (2010).
7. D. M. H. Baker, J. W. Head, C. I. Fassett, S. J. Kadish, D. E. Smith, M. T. Zuber, G. A. Neumann, The transition from complex crater to peak-ring basin on the Moon: New observations from the Lunar Orbiter Laser Altimeter (LOLA) instrument. *Icarus* **214**, 377–393 (2011).
8. H. J. Melosh, W. B. McKinnon, The mechanics of ringed basin formation. *Geophys. Res. Lett.* **5**, 985–988 (1978).
9. H. J. Melosh, *Impact Cratering: A Geologic Process.* (Oxford Univ. Press, New York, 1989).
10. J. V. Morgan, M. R. Warner, G. S. Collins, H. J. Melosh, G. L. Christeson, Peak-ring formation in large impact craters: Geophysical constraints from Chicxulub. *Earth Planet. Sci. Lett.* **183**, 347–354 (2000).
11. J. W. Head, Orientale multi-ringed basin interior and implications for the petrogenesis of lunar highland samples. *Moon* **11**, 327–356 (1974).
12. M. A. Wieczorek, R. J. Phillips, Lunar multiring basins and the cratering process. *Icarus* **139**, 246–259 (1999).
13. P. M. Muller, W. L. Sjogren, Mascons: Lunar mass concentrations. *Science* **161**, 680–684 (1968).
14. S. R. Bratt, S. C. Solomon, J. W. Head, C. H. Thurber, The deep structure of lunar basins: Implications for basin formation and modification. *J. Geophys. Res.* **90**, 3049–3064 (1985).
15. M. T. Zuber, D. E. Smith, F. G. Lemoine, G. A. Neumann, The shape and internal structure of the moon from the Clementine mission. *Science* **266**, 1839–1843 (1994).
16. F. G. R. Lemoine, D. E. Smith, M. T. Zuber, G. A. Neumann, D. D. Rowlands, A 70th degree lunar gravity model (GLGM-2) from Clementine and other tracking data. *J. Geophys. Res.* **102**, 16339–16359 (1997).
17. A. S. Konopliv, S. W. Asmar, E. Carranza, W. L. Sjogren, D. N. Yuan, Recent gravity models as a result of the Lunar Prospector mission. *Icarus* **150**, 1–18 (2001).
18. K. Matsumoto, S. Goossens, Y. Ishihara, Q. Liu, F. Kikuchi, T. Iwata, N. Namiki, H. Noda, H. Hanada, N. Kawano, F. G. Lemoine, D. D. Rowlands, An improved lunar gravity field model from SELENE and historical tracking data: Revealing the farside gravity features. *J. Geophys. Res.* **115**, E06007 (2010).
19. G. A. Neumann, M. T. Zuber, D. E. Smith, F. G. Lemoine, The lunar crust: Global structure and signature of major basins. *J. Geophys. Res.* **101**, 16841–16863 (1996).
20. Y. Ishihara, S. Goossens, K. Matsumoto, H. Noda, H. Araki, N. Namiki, H. Hanada, T. Iwata, S. Tazawa, S. Sasaki, Crustal thickness of the Moon: Implications for farside basin structures. *Geophys. Res. Lett.* **36**, L19202 (2009).
21. M. T. Zuber, D. E. Smith, M. M. Watkins, S. W. Asmar, A. S. Konopliv, F. G. Lemoine, H. J. Melosh, G. A. Neumann, R. J. Phillips, S. C. Solomon, M. A. Wieczorek, J. G. Williams, S. J. Goossens, G. Kruizinga, E. Mazarico, R. S. Park, D.-N. Yuan, Gravity field of the Moon from the Gravity Recovery and Interior Laboratory (GRAIL) mission. *Science* **339**, 668–671 (2013).
22. D. E. Smith, M. T. Zuber, G. A. Neumann, F. G. Lemoine, E. Mazarico, M. H. Torrence, J. F. McGarry, D. D. Rowlands, J. W. Head III, T. H. Duxbury, O. Aharonson, P. G. Lucey, M. S. Robinson, O. S. Barnouin, J. F. Cavanaugh, X. Sun, P. Liiva, D. Mao, J. C. Smith, A. E. Bartels, Initial observations from the Lunar Orbiter Laser Altimeter (LOLA). *Geophys. Res. Lett.* **37**, L18204 (2010).
23. M. A. Wieczorek, G. A. Neumann, F. Nimmo, W. S. Kiefer, G. J. Taylor, H. J. Melosh, R. J. Phillips, S. C. Solomon, J. C. Andrews-Hanna, S. W. Asmar, A. S. Konopliv, F. G. Lemoine, D. E. Smith, M. M. Watkins, J. G. Williams, M. T. Zuber, The crust of the Moon as seen by GRAIL. *Science* **339**, 671–675 (2013).
24. R. W. K. Potter, D. A. Kring, G. S. Collins, W. S. Kiefer, P. J. McGovern, Estimating transient crater size using the crustal annular bulge: Insights from numerical modeling of lunar basin-scale impacts. *Geophys. Res. Lett.* **39**, L18203 (2012).
25. G. S. Collins, H. J. Melosh, J. V. Morgan, M. R. Warner, Hydrocode simulations of Chicxulub crater collapse and peak-ring formation. *Icarus* **157**, 24–33 (2002).
26. H. J. Melosh, A. M. Freed, B. C. Johnson, D. M. Blair, J. C. Andrews-Hanna, G. A. Neumann, R. J. Phillips, D. E. Smith, S. C. Solomon, M. A. Wieczorek, M. T. Zuber, The origin of lunar mascon basins. *Science* **340**, 1552–1555 (2013).
27. K. Miljković, M. A. Wieczorek, G. S. Collins, M. Laneuville, G. A. Neumann, H. J. Melosh, S. C. Solomon, R. J. Phillips, D. E. Smith, M. T. Zuber, Asymmetric distribution of lunar impact basins caused by variations in target properties. *Science* **342**, 724–726 (2013).
28. H. V. Frey, Previously unknown large impact basins on the Moon: Implications for lunar stratigraphy, in *Recent Advances and Current Research Issues in Lunar Stratigraphy,* W. A. Ambrose, D. A. Williams, Eds. (Special Paper 477, Geological Society of America, Boulder, CO, 2011), pp. 53–75.
29. A. C. Cook, P. D. Spudis, M. S. Robinson, T. R. Watters, Lunar topography and basins mapped using a Clementine stereo digital elevation model. *Lunar Planet. Sci.* **33**, abstract 1281 (2002).
30. D. Stöffler, G. Ryder, B. A. Ivanov, N. A. Artemieva, M. J. Cintala, R. A. F. Grieve, Cratering history and lunar chronology. *Rev. Mineral. Geochem.* **60**, 519–596 (2006).
31. M. A. Wieczorek, R. J. Phillips, The "Procellarum KREEP Terrane": Implications for mare volcanism and lunar evolution. *J. Geophys. Res.* **105**, 20417–20430 (2000).
32. B. L. Jolliff, J. J. Gillis, L. A. Haskin, R. L. Korotev, M. A. Wieczorek, Major lunar crustal terranes: Surface expressions and crust-mantle origins. *J. Geophys. Res.* **105**, 4197–4216 (2000).
33. M. Le Feuvre, M. A. Wieczorek, Nonuniform cratering of the Moon and a revised crater chronology of the inner Solar System. *Icarus* **214**, 1–20 (2011).
34. K. A. Holsapple, K. R. Housen, A crater and its ejecta: An interpretation of Deep Impact. *Icarus* **187**, 345–356 (2007).
35. R. Gomes, H. F. Levison, K. Tsiganis, A. Morbidelli, Origin of the cataclysmic Late Heavy Bombardment period of the terrestrial planets. *Nature* **435**, 466–469 (2005).
36. W. F. Bottke, D. Vokrouhlický, D. Minton, D. Nesvorný, A. Morbidelli, R. Brasser, B. Simonson, H. F. Levison, An Archaean heavy bombardment from a destabilized extension of the asteroid belt. *Nature* **485**, 78–81 (2012).
37. D. A. Minton, J. E. Richardson, C. I. Fassett, Re-examining the main asteroid belt as the primary source of ancient lunar craters. *Icarus* **247**, 172–190 (2015).
38. R. G. Strom, R. Malhotra, T. Ito, F. Yoshida, D. A. Kring, The origin of planetary impactors in the inner solar system. *Science* **309**, 1847–1850 (2005).
39. F. G. Lemoine, S. Goossens, T. J. Sabaka, J. B. Nicholas, E. Mazarico, D. D. Rowlands, B. D. Loomis, D. S. Chinn, G. A. Neumann, D. E. Smith, M. T. Zuber, GRGM900C: A degree 900 lunar gravity model from GRAIL primary and extended mission data. *Geophys. Res. Lett.* **41**, 3382–3389 (2014).
40. M. A. Wieczorek, R. J. Phillips, Potential anomalies on a sphere: Applications to the thickness of the lunar crust. *J. Geophys. Res.* **103**, 1715–1724 (1998).
41. Y. Ishihara, T. Morota, R. Nakamura, S. Goossens, S. Sasaki, Anomalous Moscoviense basin: Single oblique impact or double impact origin? *Geophys. Res. Lett.* **38**, L03201 (2011).
42. R. J. Pike, Size-dependence in the shape of fresh impact craters on the moon, in *Impact and Explosion Cratering: Planetary and Terrestrial Implications,* D. J. Roddy, R. O. Pepin, R. B. Merrill, Eds. (Pergamon, New York, 1977), pp. 489–509.
43. R. J. Pike, P. D. Spudis, Basin-ring spacing on the Moon, Mercury and Mars. *Earth Moon Planets* **39**, 129–194 (1987).
44. D. M. H. Baker, J. W. Head, G. A. Neumann, D. E. Smith, M. T. Zuber, The transition from complex craters to multi-ring basins on the Moon: Quantitative geometric properties from Lunar Reconnaissance Orbiter Lunar Orbiter Laser Altimeter (LOLA) data. *J. Geophys. Res.* **117**, E00H16 (2012).
45. C. I. Fassett, J. W. Head, S. J. Kadish, E. Mazarico, G. A. Neumann, M. T. Zuber, D. E. Smith, Lunar impact basins: Stratigraphy, sequence and ages from superposed impact crater populations measured from Lunar Orbiter Laser Altimeter (LOLA) data. *J. Geophys. Res.* **117**, E00H06 (2012).
46. J. W. Head, Processes of lunar crater degradation: Changes in style with geologic time. *Moon* **12**, 299–329 (1975).
47. J. W. Head, Lava flooding of ancient planetary crusts: Geometry, thickness, and volumes of flooded lunar impact basins. *Moon Planets* **26**, 61–88 (1982).

48. J. L. Whitten, J. W. Head III, Detecting volcanic resurfacing of heavily cratered terrain: Flooding simulations on the Moon using Lunar Orbiter Laser Altimeter (LOLA) data. *Planet. Space Sci.* **85**, 24–37 (2013).

49. C. I. Fassett, J. W. Head, D. M. H. Baker, M. T. Zuber, D. E. Smith, G. A. Neumann, S. C. Solomon, C. Klimczak, R. G. Strom, C. R. Chapman, L. M. Prockter, R. J. Phillips, J. Oberst, F. Preusker, Large impact basins on Mercury: Global distribution, characteristics and modification history from MESSENGER orbital data. *J. Geophys. Res.* **117**, E00L08 (2012).

50. V. L. Sharpton, J. W. Head III, Stratigraphy and structural evolution of southern Mare Serenitatis: A reinterpretation based on Apollo Lunar Sounder Experiment data. *J. Geophys. Res.* **87**, 10983–10998 (1982).

51. D. H. Scott, The geologic significance of some lunar gravity anomalies. *Proc. Lunar Sci. Conf.* **5**, 3025–3036 (1974).

52. W. M. Vaughan, J. W. Head, L. Wilson, P. C. Hess, Geology and petrology of enormous volumes of impact melt on the Moon: A case study of the Orientale basin impact melt sea. *Icarus* **223**, 749–765 (2013).

53. I. Garrick-Bethell, M. T. Zuber, Elliptical structure of the lunar South Pole-Aitken basin. *Icarus* **204**, 399–408 (2009).

54. A. C. Cook, T. R. Watters, M. S. Robinson, P. D. Spudis, D. B. J. Bussey, Lunar polar topography derived from Clementine stereoimages. *J. Geophys. Res.* **105**, 12023–12033 (2000).

55. C. J. Byrne, Modeling the Moon's topographic features. *Lunar Planet. Sci.* **43**, abstract 1118 (2012).

56. C. J. Byrne, A large basin on the near side of the Moon. *Earth Moon Planets* **101**, 153–188 (2007).

57. J. C. Andrews-Hanna, S. W. Asmar, J. W. Head III, W. S. Kiefer, A. S. Konopliv, F. G. Lemoine, I. Matsuyama, E. Mazarico, P. J. McGovern, H. J. Melosh, G. A. Neumann, F. Nimmo, R. J. Phillips, D. E. Smith, S. C. Solomon, G. J. Taylor, M. A. Wieczorek, J. G. Williams, M. T. Zuber, Ancient igneous intrusions and early expansion of the Moon revealed by GRAIL gravity gradiometry. *Science* **339**, 675–678 (2013).

58. W. E. Featherstone, C. Hirt, M. Kuhn, Band-limited Bouguer gravity identifies new basins on the Moon. *J. Geophys. Res. Planets* **118**, 1397–1413 (2013).

59. C. M. Pieters, Copernicus crater central peak: Lunar mountain of unique composition. *Science* **215**, 59–61 (1982).

60. J. M. Sunshine, S. Besse, N. E. Petro, C. M. Pieters, J. W. Head, L. A. Taylor, R. L. Klima, P. J. Isaacson, J. W. Boardman, R. C. Clark; M³ Team, Hidden in plain sight: Spinel-rich deposits on the nearside of the Moon as revealed by Moon Mineralogy Mapper (M³). *Lunar Planet. Sci.* **41**, abstract 1508 (2010).

61. S. Yamamoto, R. Nakamura, T. Matsunaga, Y. Ogawa, Y. Ishihara, T. Morota, N. Hirata, M. Ohtake, T. Hiroi, Y. Yokota, J. Haruyama, A new type of pyroclastic deposit on the Moon containing Fe-spinel and chromite. *Geophys. Res. Lett.* **40**, 4549–4554 (2013).

62. K. Miljković, M. A. Wieczorek, G. S. Collins, S. C. Solomon, D. E. Smith, M. T. Zuber, Excavation of the lunar mantle by basin-forming impact events on the Moon, *Earth Planet. Sci. Lett.* **409**, 243–251 (2015).

63. R. W. Wichman, P. H. Schultz, The Crisium basin: Implications of an oblique impact for basin ring formation and cavity collapse. *Geol. Soc. Am. Spec. Pap.* **293**, 61–72 (1992).

64. P. H. Schultz, A. M. Stickle, Arrowhead craters and tomahawk basins: Signatures of oblique impacts at large scales. *Lunar Planet. Sci.* **42**, abstract 2611 (2011).

65. Q. Huang, J. Ping, X. Su, R. Shu, G. Tang, New features of the Moon revealed and identified by CLTM-s01. *Sci. China Ser. G Phys. Mech. Astron.* **52**, 1815–1823 (2009).

The following resources related to this article are available online at http://advances.sciencemag.org. (This information is current as of December 22, 2015):

Updated information and services, including high-resolution figures, can be found in the online version of this article at:
http://advances.sciencemag.org/content/1/9/e1500852.full

Supporting Online Material can be found at:
http://advances.sciencemag.org/content/suppl/2015/10/27/1.9.e1500852.DC1

This article **cites 60 articles,** 11 of which you can be accessed free:
http://advances.sciencemag.org/content/1/9/e1500852#BIBL